Inorganic Chemistry

Article

pubs.acs.org/IC

Multidimensional Network Structures and Versatile Magnetic Properties of Intermolecular Compounds of a Radical−Anion Ligand, [1,2,5]Thiadiazolo[3,4-*f*][1,10]phenanthroline 1,1-Dioxide

Yoshiaki Shuku,[†] Rie Suizu,[†,‡] Alex Domingo,[§] Carmen J. Calzado,[⊥] Vincent Robert,*[,§] and Kunio Awaga*[,†]

[†]Department of Chemistry & Research Centre for Materials Science, Nagoya University, Furo-cho, Chikusa, 464-8602 Nagoya, Japan

[§]Laboratoire de Chimie Quantique, Institut de Chimie UMR 7177, Université de Strasbourg, 1 rue Blaise Pascal, 67000 Strasbourg, France

[⊥]Departamento de Química Física, Universidad de Sevilla, c/Prof. García González, s/n. E-41012 Sevilla, Spain

Supporting Information

ABSTRACT: The crystal structures and magnetic properties of seven kinds of [1,2,5]thiadiazolo[3,4-*f*][1,10]phenanthroline 1,1-dioxide ($tdapO_2$) radical−anion salts, namely, K·$tdapO_2$, K·$tdapO_2$·0.5MeCN, K·$(tdapO_2)_2$, Rb·$(tdapO_2)_2$, Cs_7·$(tdapO_2)_6$·ClO_4, $(NH_4)_2$·$tdapO_2$·I, and Hppda·$tdapO_2$·MeCN, were investigated. Single-crystal X-ray analyses of these radical−anion salts revealed formation of π-stacking columns and the presence of intercolumnar coordination bonding or hydrogen bonding. The intermolecular magnetic coupling constants in these salts range from strong antiferromagnetic (J/k_B = −310 K) to ferromagnetic (J/k_B = 24 K). Ab initio calculations performed on the nearest-neighbor radical pairs in the π-stacking columns suggested that the magnetic interactions are strongly governed by the overlap between the two anionic radical species and well explain the observed ferromagnetic and antiferromagnetic interactions. In addition, calculations of a hypothetical oxygen-less tdap analogue suggested that the presence of oxygen in $tdapO_2$ significantly reduces the hopping integral and enhances the probability of ferromagnetic interaction.

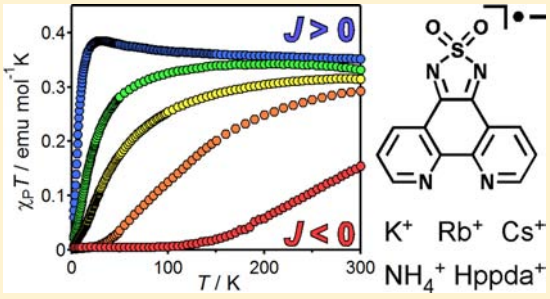

I. INTRODUCTION

The electrical and magnetic properties of molecule-based materials have been extensively studied, and versatile phenomena, such as semiconduction, conduction, superconduction, nonlinear transport, magnetic ordering, paramagnetic−diamagnetic transitions, and low-dimensional magnetism, have been discovered.[1] In these research fields, open-shell radical species have been widely employed, because the unpaired electrons are potential charge carriers and magnetization sources. In contrast to the chemical variety of cationic and neutral radicals, however, development of radical−anion species has been very limited, probably because of their instability (oxidation) under ambient (oxygen) conditions.

The most representative stable radical−anions are $TCNQ^-$ (7,7,8,8-tetracyanoquinodimethane), $TCNE^-$ (tetracyanoethylene), and $DCNQI^-$ (3,6-bis(cyanoimino)cyclohexa-1,4-diene), which have been shown to form functional charge transfer compounds with various radical−cations and metal ions.[2] It is notable that these anions have the duality of being both radical−anions and ligands, and they often form a 3D network structure involving $\pi-\pi$ interactions and coordination bonds.[1a,3] It is therefore important to develop a methodology to stabilize radical−anion species and expand their chemical variety.

In our previous work, we synthesized an electron acceptor molecule, [1,2,5]thiadiazolo[3,4-*f*][1,10]phenanthroline 1,1-dioxide (abbreviated as $tdapO_2$; see Scheme 1), which was designed to possess a stable radical−anion species. The strong electron-withdrawing property of the thiadiazole dioxide moiety enhances the acceptor ability of $tdapO_2$.[4] In addition, the phenanthroline and thiadiazole dioxide moieties at the molecular ends operate as ligands, which realize multidimensional interactions. We reported the crystal structures and the magnetic properties of the monovalent and mixed-valent potassium radical−anion salts of $tdapO_2$, namely, K·$tdapO_2$ and K·$(tdapO_2)_2$.[5]

In the present paper, we describe the crystal structures and magnetic properties of various intermolecular compounds based on $tdapO_2$ (Scheme 1), which exhibit $tdapO_2$ valences of 0, −0.5, −1, and −2, and include coordination bonding or hydrogen bonding. The magnetic behavior ranges from strong antiferromagnetic to ferromagnetic, and the origin of this behavior is rationalized using different experimental techniques and ab initio calculations.

Received: April 30, 2013
Published: August 12, 2013

dx.doi.org/10.1021/ic401078z | Inorg. Chem. 2013, 52, 9921−9930

Scheme 1. Intermolecular Compounds of $tdapO_2$, Prepared by the Diffusion Method (blue arrow) or by Electrochemical Reduction (red arrow)[a]

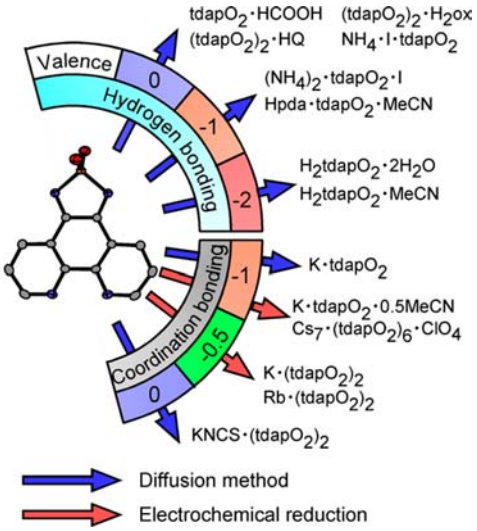

[a]The outer circle shows the valences of the $tdapO_2$ units and the inner circle the intermolecular interaction motif as either coordination or hydrogen bonding in nature.

II. EXPERIMENTAL SECTION

General Considerations. Molecular $tdapO_2$ was prepared according to a reported method.[5] The $tdapO_2$-related compound tdap ([1,2,5]thiadiazolo[3,4-*f*][1,10]phenanthroline, shown in Figure S1, Supporting Information) was also prepared according to the reported method.[6] All other chemicals were purchased and used as received. During crystallization of the radical−anion salts, the cells were kept under N_2 atmosphere and the solvent was purged with N_2 before use. The potassium salts, K·$tdapO_2$ and K·$(tdapO_2)_2$, were synthesized following the reported method.[5] Crystals used for magnetic measurements were removed from the mother liquor, rinsed with acetonitrile (MeCN), and dried under N_2 gas flow. All compounds and salts described in the present paper are stable even under ambient conditions. The appearance of the crystals did not degrade over a period of at least several months when stored in a refrigerator. ***Caution!*** *Although no problem was encountered in this work, perchlorate salts are potentially explosive and should be handled with care.*

Preparation of K·$tdapO_2$·0.5MeCN. Black needle-shaped crystals of K·$tdapO_2$·MeCN were obtained by galvanostatic electrocrystallization (0.5 μA) of a saturated electrolyte solution of MeCN containing $tdapO_2$ (1 mM). Potassium perchlorate ($KClO_4$) was used as an electrolyte. After 1 month, black needle-shaped crystals had grown. A higher concentration of $tdapO_2$ gives thinner needle-shaped crystals of the potassium salt with a different formula, K·$(tdapO_2)_2$, which can be differentiated based on their appearance. Crystal data: $C_{13}H_{7.5}N_{4.5}O_2SK$; monoclinic; *C*2/*c* (no. 15); a = 17.942(3) Å, b = 7.3043(13) Å, c = 20.557(4) Å; β = 103.021(2)°; V = 2624.8(8) Å^3; R [$I > 2\sigma(I)$] = 0.0344; wR_2 [all] = 0.1009; GOF = 1.066.

Preparation of Rb·$(tdapO_2)_2$. Rb·$(tdapO_2)_2$ was obtained by galvanostatic electrocrystallization (0.5 μA) of a saturated electrolyte solution of MeCN containing an excess amount of $tdapO_2$. Rubidium perchlorate ($RbClO_4$) was used as an electrolyte. After 2−3 weeks, black thin needle-shaped crystals of the salt had grown in the formed purple solution. Crystal data: $C_{24}H_{12}N_8O_4S_2Rb$; monoclinic; $P2_1/n$ (no. 14); a = 9.8300(17) Å, b = 19.415(3) Å, c = 13.0121(2) Å; β = 111.173(2)°; V = 2317.3(7) Å^3; R [$I > 2\sigma(I)$] = 0.0544; wR_2 [all] = 0.1399; GOF = 1.090.

Preparation of Cs_7·$(tdapO_2)_6$·ClO_4. Black needle-shaped crystals of Cs_7·$(tdapO_2)_6$·ClO_4 were obtained by galvanostatic electrocrystallization (0.5 μA) of a saturated electrolyte solution of MeCN containing $tdapO_2$ (1 mM). Cesium perchlorate ($CsClO_4$) was used as an electrolyte. After 2 weeks, black needle-shaped crystals had grown. Crystal data: $C_{72}H_{36}N_{24}O_{16}S_6ClCs_7$; trigonal; $R\bar{3}$ (no. 148); a = 28.5168(5) Å, c = 8.2245(2) Å; V = 5792.2(2) Å^3; R [$I > 2\sigma(I)$] = 0.0241; wR_2 [all] = 0.0531; GOF = 1.086.

Preparation of $(NH_4)_2$·$tdapO_2$·I. Black needle-shaped crystals of $(NH_4)_2$·$tdapO_2$·I were obtained by the slow diffusion method using an H-shaped glass cell. $TdapO_2$ and an excess amount of ammonium iodide (NH_4I) were placed into different sides of the H-shaped cell. MeCN was added slowly to the cell. After 1−2 months, black needle crystals of $(NH_4)_2$·$tdapO_2$·I were obtained. Crystal data: $C_{12}H_{14}N_6O_2SI$; triclinic; $P\bar{1}$ (no. 2); a = 7.4094(16) Å, b = 9.741(2) Å, c = 12.500(3) Å; α = 105.5963(18)°, β = 93.308(3)°, γ = 112.3471(16)°; V = 790.6(3) Å^3; R [$I > 2\sigma(I)$] = 0.0207; wR_2 [all] = 0.0519; GOF = 1.095.

Preparation of Hppda·$tdapO_2$·MeCN. Black needle-shaped crystals of Hppda·$tdapO_2$·MeCN were obtained by the slow diffusion method using an H-shaped glass cell purged with N_2 gas. An excess amount of *p*-phenylenediamine (ppda) and $tdapO_2$ were placed into each side of the H-shaped cell, individually. MeCN was then added slowly to the cell. After 1−2 weeks, black needle-shaped crystals of Hppda·$tdapO_2$·MeCN were obtained. Crystal data: $C_{20}H_{18}N_7O_2S$; orthorhombic; *Pnma* (no. 62); a = 15.728(6) Å, b = 6.839(2) Å, c = 18.464(7) Å; V = 1985.9(13) Å^3; R [$I > 2\sigma(I)$] = 0.0885; wR_2 [all] = 0.1925; GOF = 1.233.

Electrochemical Measurements. Cyclic voltammetry was performed using a Hokuto Denko HZ-5000 Automatic Polarization System at room temperature. A conventional three-electrode cell was used, which consisted of a glassy carbon disk (3 mm diameter) as the working electrode and a Pt wire as the counter electrode. A silver wire in an MeCN solution of 0.01 M silver nitrate ($AgNO_3$) and 0.1 M tetra-*n*-butylammonium perchlorate (*n*-Bu_4NClO_4) was used as the Ag/Ag^+ reference electrode. Solutions were deoxygenated by passing dry nitrogen through them before measurements. Ferrocene (Fc) was used as an internal standard, and the potential was converted to the ferrocene scale (Fc/Fc^+). In the present report, we found a redox peak of tdap by applying a higher voltage than that previously reported.[5]

EPR Measurement and Its Theoretical Fitting. Electron paramagnetic resonance (EPR) measurements were carried out on a JEOL JES-FA 200 ESR Spectrometer. For solution measurements of the electrochemically reduced $tdapO_2$, the solvent was degassed and the sample folder was purged with N_2 gas and sealed. A dichloromethane (CH_2Cl_2) solution of reduced $tdapO_2$ salt was prepared as follows. An MeCN solution of the $tdapO_2$ (1 mM) with *n*-Bu_4NClO_4 (100 mM) was reduced by the potentiostatic method (−0.6 V vs Ag/Ag^+). This MeCN solution was then evaporated to dryness, and the residue was dissolved in CH_2Cl_2. This CH_2Cl_2 solution of reduced $tdapO_2$ was degassed by the frozen degas technique and sealed in a quartz cell under a vacuum before measurements. Simulation for the solution EPR was carried out using the software package Isotropic simulation Iso Simu/FA, Version 2.2.0.

X-ray Structural Analyses. X-ray investigations were performed at 173 K. Crystals were mounted on a loop using oil (CryoLoop, Immersion Oil, Type B; Hampton Research Corp.) and set on a Rigaku RA-Micro007 with a Saturn CCD detector using graphite-monochromated Mo Kα radiation (λ = 0.710690 Å) under a cold nitrogen stream. Frame data were integrated and corrected for absorption with the Rigaku/MSC CrystalClear package.[7] Structures were solved by direct methods and standard difference map techniques and refined with full-matrix least-squares procedures on F^2 using the Rigaku/MSC CrystalStructure package.[7,8] Anisotropic refinement was applied to all non-hydrogen atoms. Hydrogen atoms in formic acid (HCOOH) of $tdapO_2$·HCOOH, oxalic acid (H_2ox) of $tdapO_2$·H_2ox, and acetonitrile of K·$tdapO_2$·0.5MeCN could not be located. All other hydrogen atoms on nitrogen and oxygen atoms were located in a difference Fourier map and refined isotropically. All hydrogen atoms on carbon atoms were placed at calculated positions and refined using a riding model. CCDC 819975 (K·$tdapO_2$), CCDC 819974 (K·$(tdapO_2)_2$), CCDC 932267 (K·$tdapO_2$·0.5MeCN), CCDC 932268 (Rb·$(tdapO_2)_2$), CCDC 932269 (Cs_7·$(tdapO_2)_6$·ClO_4), CCDC 819972 ($(NH_4)_2$·$tdapO_2$·I), CCDC 819973 (Hppda·$tdapO_2$·MeCN),

dx.doi.org/10.1021/ic401078z | *Inorg. Chem.* 2013, 52, 9921−9930

CCDC 932270 ($tdapO_2$·HCOOH), CCDC 932271 (($tdapO_2$)$_2$·H_2ox), CCDC 932272 (($tdapO_2$)$_2$·HQ), CCDC 932273 (NH_4I·$tdapO_2$), CCDC 932274 (KNCS·($tdapO_2$)$_2$), CCDC 932275 (H_2tdapO_2·$2H_2O$), and CCDC 932276 (H_2tdapO_2·MeCN) contain supplementary crystallographic data for this paper. These data can be obtained free of charge from The Cambridge Crystallographic Data Centre via www.ccdc.cam.ac.uk/data_request/cif.

Magnetic Measurements. Magnetic susceptibility measurements were carried out on polycrystalline samples on a MPMS-XL Quantum Design magnetometer. All of the measurements used a plastic straw as the sample folder. Measurements for K·$tdapO_2$, K·($tdapO_2$)$_2$, K·$tdapO_2$·0.5MeCN, Rb·($tdapO_2$)$_2$, Cs_7·($tdapO_2$)$_6$·ClO_4, (NH_4)$_2$·$tdapO_2$·I, and Hppda·$tdapO_2$·MeCN were performed under 3 T in the temperature range of 2−300 K. For K·($tdapO_2$)$_2$ and Rb·($tdapO_2$)$_2$ measurements were also performed under 0.05 T in the temperature range 2−50 K. Temperature dependences of the paramagnetic susceptibilities χ_p of the radical−anion salts were calculated with diamagnetic susceptibilities obtained as fitting parameters. Magnetization curves for K·($tdapO_2$)$_2$ and Rb·($tdapO_2$)$_2$ were measured at 2, 5, 10, 15, 20, and 30 K under a magnetic field range from −5 to 5 T.

Computational Detail of Wave Function Calculations. To complement the experimental data analysis, we considered that theoretical calculations would be desirable to decipher the origin of the different magnetic behaviors. From the X-ray structures, the synthetic systems can be considered as regular or alternating $S = 1/2$ quasi-one-dimensional materials. Therefore, exchange coupling constants J were calculated as the energy difference between the singlet $E(S)$ and triplet $E(T)$ low-lying states $2J = E(S) - E(T)$ of dimeric units built on nearest-neighbor radicals. Wave-function-based calculations were preferred to simultaneously access the spin-state ordering within these dimeric units and partition the ferro- and antiferromagnetic contributions. Considering the presence of two unpaired electrons in a dimeric unit, three singlet and one triplet low-lying spin states were anticipated. The four determinants with $M_s = 0$ span the so-called valence model space. Useful information can be extracted from the singlet and triplet wave functions determined by means of ab initio calculations. Indeed, through their projections onto the valence model space, the effective Hamiltonian theory allows for quantification of the effective hopping integral (t), on-site repulsion (U), and direct exchange parameters (K).[9] The ferro- and antiferromagnetic contributions can be estimated following the $2J = 2K - 4t^2/U$ relationship, with the $2K$ term representing the ferromagnetic contribution and the $-4t^2/U$ term the antiferromagnetic one. Thus, complete active space self-consistent field (CASSCF)[10] calculations including 2 electrons in 2 molecular orbitals, namely, CAS[2,2], were performed upon dimers using the Molcas7.2 package.[11a] From the CASSCF wave function of the triplet state, the Mulliken spin populations were calculated on each atomic center (Figure S2a, Supporting Information).

Guided by the X-ray structures, we extracted one or two pairs of radicals without performing any geometry optimization to evaluate the corresponding exchange coupling constant values and effective parameters. The sulfur, oxygen, carbon, and nitrogen atoms were described with ANO RCC-type DZP basis sets.[11b] A minimal basis set (8s)/[1s] was used for the hydrogen atoms. The systems that contained potassium cations, namely, K·$tdapO_2$, K·($tdapO_2$)$_2$, and K·$tdapO_2$·0.5MeCN, used Ab Initio Model Potentials (AIMP) to represent the potassium cations in the computational model.[12]

Beyond the CASSCF level, important electron−electron interactions were explicitly treated using the Difference Dedicated CI (DDCI) framework as implemented in the CASDI code.[13] On top of the CASSCF wave function, additional determinants are introduced in a variational treatment that follows the traditional hierarchy given by the number of generated holes (h) and particles (p). The procedure we used has been described previously in the literature and leads to quantitative estimations of the singlet/triplet splittings when the highest level of correlation is reached within this framework.[14] In practice, a single set of MOs must be used to afford a systematic suppression of the numerous 2h−2p excitations. All our calculations were performed using both the CAS[2,2]SCF singlet and the triplet MOs to confirm the invariance of the DDCI calculations with respect to the set of MOs employed.

III. ELECTROCHEMISTY AND SPIN DENSITY DISTRIBUTION

The electrochemical properties of $tdapO_2$ were investigated by cyclic voltammetry (CV). Figure 1 shows the CV curve of

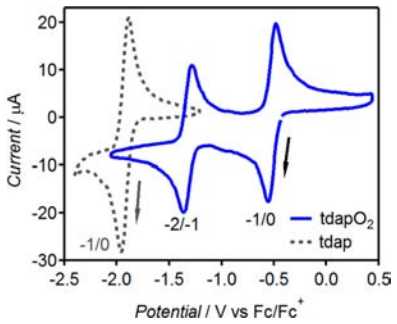

Figure 1. CV curves of $tdapO_2$ and tdap (1 mM) in MeCN solutions of n-Bu_4N·ClO_4 (100 mM) at a scan rate of 100 mV s^{-1}.

$tdapO_2$ in MeCN (solid line), together with that of the related compound, tdap (broken line). The curve for $tdapO_2$ shows two reversible reduction peaks at −0.520 and −1.32 V vs Fc^+/Fc, whereas tdap exhibits a single reduction peak at a higher voltage of −1.93 V. Oxidation of the sulfur in the thiadiazole ring notably reduces the reduction potential and stabilizes the mono- and dianionic species of $tdapO_2$. The acceptor ability of $tdapO_2$ is comparable to those of the halogen-substituted p-benzoquinones.[15] Furthermore, the small potential separation ($\Delta E_{1/2}$) between the two reduction peaks of $tdapO_2$ indicates an extended delocalization of the LUMO orbital, as observed for nickel bisdithiolene.[16] The monoanion radical is well distributed over the molecular skeleton, thereby decreasing the Coulombic repulsion for the subsequent reduction.

Solution EPR measurements for the electrochemically reduced $tdapO_2$ were carried out in CH_2Cl_2 solution. Figure 2a shows the hyperfine structure of monoanionic $tdapO_2$ (red trace), which consists of 89 peaks. This complex feature indicates a delocalization of the unpaired electron over the whole molecular skeleton. The black trace in this figure shows the theoretical best fit with the following parameters: g = 2.0032, two N ($I = 1$) with a_N = 0.349 mT, two N ($I = 1$) with a_N = 0.025 mT, two H ($I = 1/2$) with a_H = 0.152 mT, two H ($I = 1/2$) with a_H = 0.148 mT, and two H ($I = 1/2$) with a_H = 0.05 mT, where g is the g factor, I is the nuclear spin quantum number, and a_N and a_H are the hyperfine coupling constants for nitrogen and hydrogen, respectively. The spin density distribution on the $tdapO_2$ radical−anion was estimated using McConell's equations, $a_H = Q_C \times \rho_C$ and $a_N = Q_N \times \rho_N$, where ρ_C and ρ_N are the spin densities on the carbon and nitrogen, respectively, and Q_C and Q_N are their corresponding proportional constants.[17] Using the equations and the empirically derived constants (Q_C = −2.45 mT[18] and Q_N = +2.5 mT[19]), the spin density distribution on the molecular skeleton of the $tdapO_2$ radical−anion was calculated. A comparison between the theoretically and the experimentally calculated spin populations of $tdapO_2$ radical−anion (Figure S2, Supporting Information) showed good agreement.

dx.doi.org/10.1021/ic401078z | Inorg. Chem. 2013, 52, 9921−9930

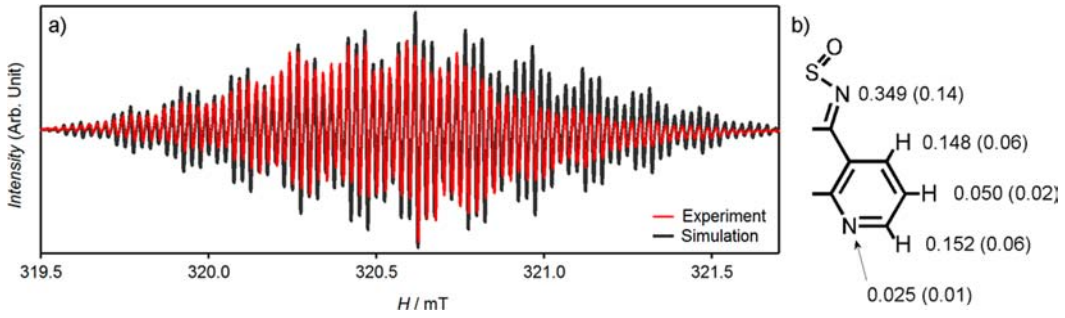

Figure 2. (a) EPR hyperfine structures of the monoanionic $tdapO_2$ in dichloromethane: observation (red) and simulation (black). (b) Hyperfine coupling constants in units of mT, and the estimated spin densities on the nitrogen and carbon atoms (in parentheses).

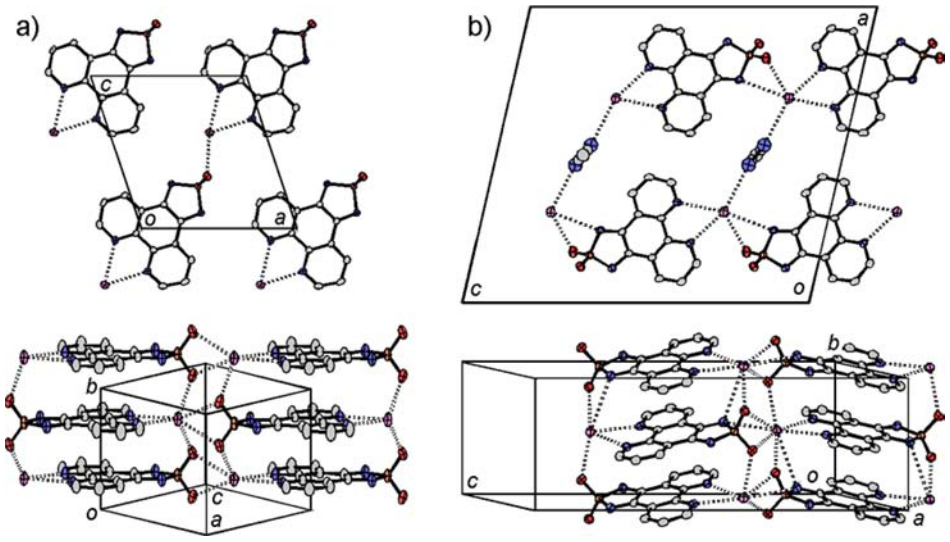

Figure 3. Crystal structures of K·$tdapO_2$ (a) and K·$tdapO_2$·0.5MeCN (b). Broken lines show the coordination bonds.

IV. CRYSTAL STRUCTURES

We carried out X-ray crystal analyses for the 14 kinds of intermolecular compounds and salts of $tdapO_2$ shown in Scheme 1, though the crystal structures of $tdapO_2$ and its monovalent and mixed-valent potassium salts were reported in ref 5. These compounds were prepared by the diffusion method or electrochemical reduction, as indicated by the blue and red arrows in Scheme 1. In these compounds, the $tdapO_2$ valences varied among the values 0, −0.5, −1, and −2. In addition, the packing motif in the crystal structure seemed to be governed by coordination bonding or hydrogen bonding.

Single-crystal X-ray analyses for the series of the $tdapO_2$ intermolecular compounds and salts revealed a characteristic relation between the bond lengths and the valence of $tdapO_2$. Figure S3 (Supporting Information) shows a comparison of selected bond lengths among the 14 compounds, in which the values were normalized by the corresponding bond lengths of the unadulterated $tdapO_2$. There was an obvious difference in bond lengths, depending on the different reduction states of 0, −1, and −2. Note that the crystal structures of the mixed-valent compounds, K·$(tdapO_2)_2$ and Rb·$(tdapO_2)_2$, consist of crystallographically independent neutral and monoanionic molecules.

Diverse structures are found in the intermolecular compounds of $tdapO_2$. The crystal structures and selected bond distances of the neutral $tdapO_2$ compounds $tdapO_2$·HCOOH, $(tdapO_2)_2$·H_2ox, $(tdapO_2)_2$·HQ (HQ = hydroquinone), NH_4I·$tdapO_2$, and KNCS·$(tdapO_2)_2$ and the divalent $tdapO_2$ salts H_2tdapO_2·$2H_2O$ and H_2tdapO_2·MeCN are shown in Figures S4−S10 and Table S2−S8 (Supporting Information). These intermolecular compounds exhibit partial π overlaps, and their structures are governed by hydrogen bonding between the proton donors and $tdapO_2$ or coordination bonding between the potassium ion and $tdapO_2$. Figures 3 and 5−8 show the crystal structures of the radical−anion salts of $tdapO_2$, namely, K·$tdapO_2$, K·$tdapO_2$·0.5MeCN, K·$(tdapO_2)_2$, Rb·$(tdapO_2)_2$, Cs_7·$(tdapO_2)_6$·ClO_4, $(NH_4)_2$·$tdapO_2$·I, and Hppda·$tdapO_2$·

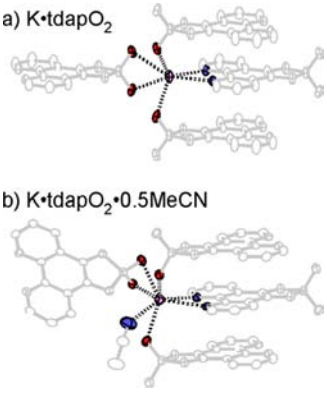

Figure 4. Coordination geometry of K·$tdapO_2$ (a) and K·$tdapO_2$·0.5MeCN (b).

dx.doi.org/10.1021/ic401078z | Inorg. Chem. 2013, 52, 9921−9930

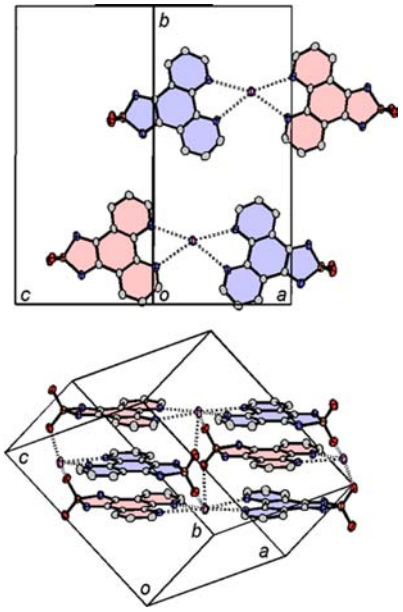

Figure 5. Crystal structure of Rb·$(tdapO_2)_2$. Broken lines show the coordination bonds.

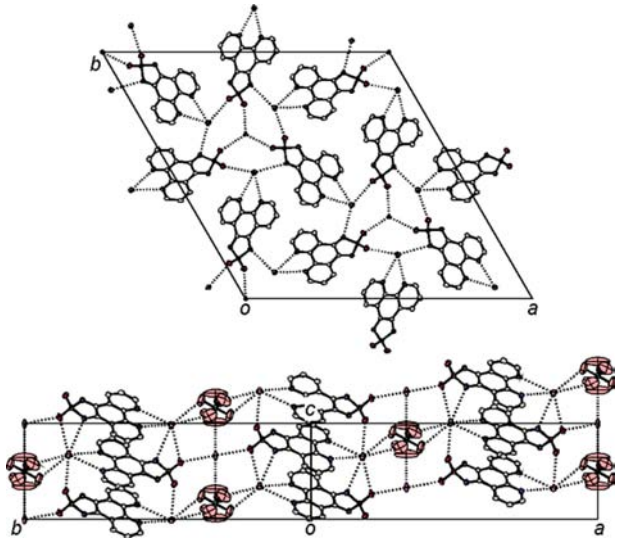

Figure 6. Crystal structure of Cs_7·$(tdapO_2)_6$·ClO_4. Broken lines show the coordination bonds.

MeCN. The intermolecular π overlaps in these crystals are shown in Figure 11. A common feature of these crystals is the presence of π-stacking columns and intercolumnar coordination or hydrogen bonds which are formed between the phenanthroline and/or thiadiazole dioxide moieties of $tdapO_2$ and their counterparts in the intermolecular compounds.

K·tdapO$_2$ and K·tdapO$_2$·0.5MeCN. As a 1:1 salt of potassium and $tdapO_2$, we obtained the solvated and nonsolvated forms. The nonsolvated form K·$tdapO_2$, which has already been reported in ref 5, crystallizes in the $P2_1/n$ space group (Figure 3a). The structure consists of a π-stacking column along the b axis with an interplanar distance of 3.30 Å. Along the $a + c$ direction there is a coordination polymer chain formed by the contacts between the thiadiazole moiety and the potassium ion and between the phenanthroline moiety and potassium ion. The solvated form, K·$tdapO_2$·0.5MeCN, crystallizes in the $C2/c$ space group. Figure 3b shows the

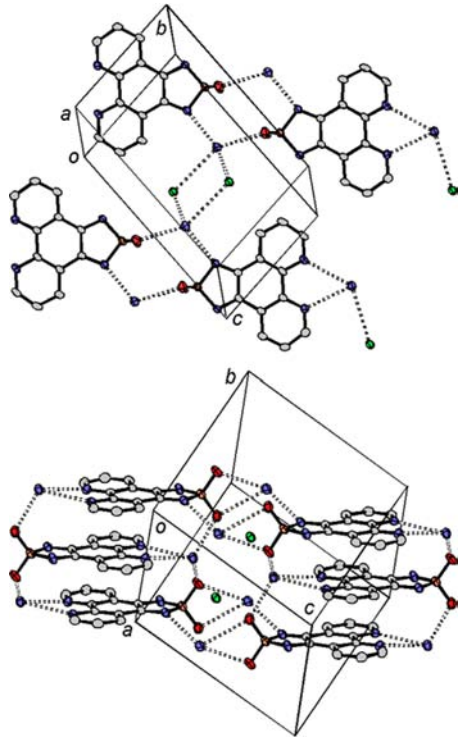

Figure 7. Crystal structure of $(NH_4)_2$·$tdapO_2$·I. Broken lines show the hydrogen bonds.

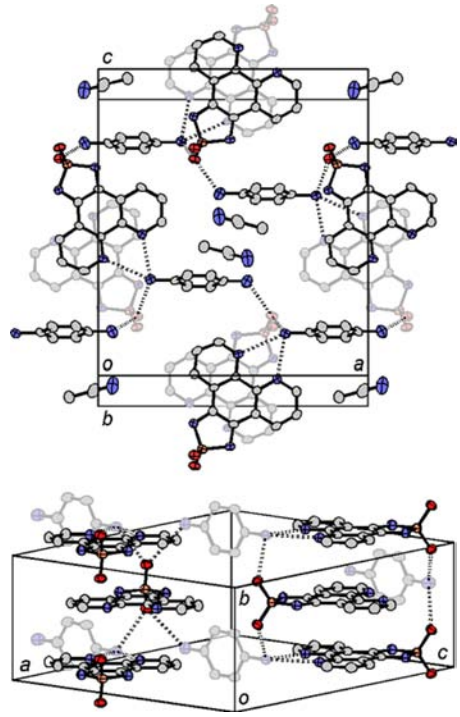

Figure 8. Crystal structure of Hppda·$tdapO_2$·MeCN. Broken lines show the hydrogen bonds.

crystal structure, which consists of a 2D layer formed by π stacking along the a axis and a coordinate bonding chain along the c axis. The 2D layers are connected by coordination bonds of MeCN molecules which are located with positional disorder between the two potassium ions. The π-overlap motif of the solvated form is significantly different from that of the

dx.doi.org/10.1021/ic401078z | Inorg. Chem. 2013, 52, 9921−9930

Table 1. Interplanar Distances and Magnetic Exchange Coupling Constants (J_1 and zJ_2) from the Theoretical Fits of Experimental Data, and J and Corresponding t, K, and U Parameters from DDCI Calculations Performed upon Pairs of Radical Units

		experimental data		computational calculation			
		interplanar distance/Å	$J_1k_B^{-1}$/K ($zJ_2k_B^{-1}$/K)	$J_{calcd}k_B^{-1}$/K	tk_B^{-1}/K	Kk_B^{-1}/K	Uk_B^{-1}/K
K·tdapO$_2$		3.30	−13[a]	17	72	23	30 522
K·tdapO$_2$·0.5MeCN	(i)	3.36	−110[b]	−100	1352	26	29 355
	(ii)	3.42		8	237	13	30 118
K·(tdapO$_2$)$_2$	(i)	3.29	−20[a]				
	(ii)	3.29					
Rb·(tdapO$_2$)$_2$	(i)	3.29	−29[a]				
	(ii)	3.31					
Cs$_7$·(tdapO$_2$)$_6$·ClO$_4$	(i)	3.13	−310[b]				
	(ii)	3.36					
(NH$_4$)$_2$·tdapO$_2$·I	(i)	3.44	24[c]	13	142	17	30 709
	(ii)	3.35	(−7.9)[d]	6	208	13	30 876
Hppda·tdapO$_2$·MeCN		3.42	5.6[e] (−2.2)[f]	13	85	17	30 745
Hppda·tdap·MeCN		hypothetical system		−4	791	32	34 533

[a]Bonner−Fisher model. [b]Bleaney−Bower Model. [c]Ferromagnetic dimer. [d]Antiferromagnetic interdimer. [e]Ferromagnetic chain. [f]Antiferromagnetic interchain.

nonsolvated form (Figure 11a and 11b), presumably due to the geometrical difference around the potassium ions (Figure 4a and 4b).

K·(tdapO$_2$)$_2$ and Rb·(tdapO$_2$)$_2$. The potassium and rubidium salts of tdapO$_2$ in a 1:2 composition ratio are isostructural and crystallize in the $P2_1/n$ space group. Figure 5 shows the crystal structure of Rb·(tdapO$_2$)$_2$. There are two crystallographically independent tdapO$_2$ molecules, whose valences are estimated as 0 (blue) and −1 (red) from their bond lengths. A π-stacking column along the $a + c$ axis is formed by an alternation of the neutral and anionic tdapO$_2$ molecules with interplanar distances of ca. 3.29 (i) and 3.31 Å (ii). A rubidium ion is tweezered by the phenanthroline moieties of the coplanar neutral and anionic tdapO$_2$ molecules in different π-stacking columns and capped by the two thiadiazole dioxide moieties from both sides of the plane.

Cs$_7$·(tdapO$_2$)$_6$·ClO$_4$. This compound crystallizes in the $R\bar{3}$ space group, in which there are seven crystallographically nonequivalent cesium ions (one is on the 3-fold rotoinversion axis, and the others are on the general positions), one perchlorate ion, and six crystallographically equivalent tdapO$_2$ molecules. Figure 6 shows the projections of the crystal structure along the c axis and onto the [110] direction. The positions of the oxygen atoms of the ClO$_4$ ion are disordered, and their occupancies are fixed to 0.5. It is notable that the six tdapO$_2$ radical−anions form a so-called "Kagome lattice" in the ab plane, which has recently attracted much attention as a highly spin-frustrated system.[20] They also form a strongly alternated π-stacking column along the c axis with the interplanar distances of 3.13 (i) and 3.36 Å (ii).

(NH$_4$)$_2$·tdapO$_2$·I. The ammonium salt of tdapO$_2$ with a chemical formula of (NH$_4$)$_2$·tdapO$_2$·I, crystallizes in the $P\bar{1}$ space group. Figure 7 shows views of the crystal structure consisting of an alternating π-stacking column with interplanar distances of 3.44 (i) and 3.35 Å (ii). Both the phenanthroline and the thiadiazole dioxide moieties form hydrogen bonds with different ammonium ions (Figure S11a, Supporting Information), indicating the proton-accepting ability of the tdapO$_2$ radical−anion. Between the π-stacking columns of tdapO$_2$, the ions, NH$_4^+$ and I$^-$, and the proton-accepting moieties of tdapO$_2$ form a 2D hydrogen bonding network.

Hppda·tdapO$_2$·MeCN. The acid−base intermolecular compound, Hppda·tdapO$_2$·MeCN, crystallizes in the *Pnma* space group. The crystal structure, shown in Figure 8, consists of a regular π-stacking of tdapO$_2$ along the b axis with an interplanar distance of 3.42 Å. Though it is hard to determine the location of the protons, the bond lengths of the tdapO$_2$ molecule and the surrounding geometry around ppda (Figure S11b, Supporting Information) strongly suggest that the valence of tdapO$_2$ is −1 and the ppda is protonated. Both the phenanthroline and the thiadiazole dioxide moieties form hydrogen bonds with different Hppda cations, making a 3D hydrogen-bonding network.

Neutral Intermolecular Compounds and Divalent Salts of tdapO$_2$. The crystal structures of the neutral tdapO$_2$ intermolecular compounds, namely, tdapO$_2$·HCOOH, (tdapO$_2$)$_2$·H$_2$ox, (tdapO$_2$)$_2$HQ, NH$_4$·I·tdapO$_2$, and KNCS·(tdapO$_2$)$_2$, and the divalent tdapO$_2$ salts, namely, H$_2$tdapO$_2$·2H$_2$O and H$_2$tdapO$_2$·MeCN, are shown in Figures S4−S10 (Supporting Information). In these compounds, hydrogen bonding between proton donors and tdapO$_2$ molecules and coordination bonding between potassium ions and tdapO$_2$ molecules are found. The KNCS·(tdapO$_2$)$_2$ formed a 1D zigzag chain structure consisting of π dimers of tdapO$_2$ and coordination bonding to the potassium ions (Figure S8, Supporting Information). The divalent tdapO$_2$ salts form a hydrogen-bonding network structure as shown in Figures S9 and S10 (Supporting Information). The crystal structure of H$_2$tdapO$_2$·2H$_2$O consists of a π-stacking column with a relatively long interplanar distance of 3.46 Å.

V. MAGNETIC PROPERTIES

The temperature dependences of the magnetic susceptibilities of the radical−anion salts of tdapO$_2$ were examined in the temperature range of 2−300 K under a magnetic field of 3 T, though the data for K·tdapO$_2$ and K·(tdapO$_2$)$_2$ had been reported previously in ref 5. The obtained magnetic parameters are listed in Table 1.

dx.doi.org/10.1021/ic401078z | Inorg. Chem. 2013, 52, 9921−9930

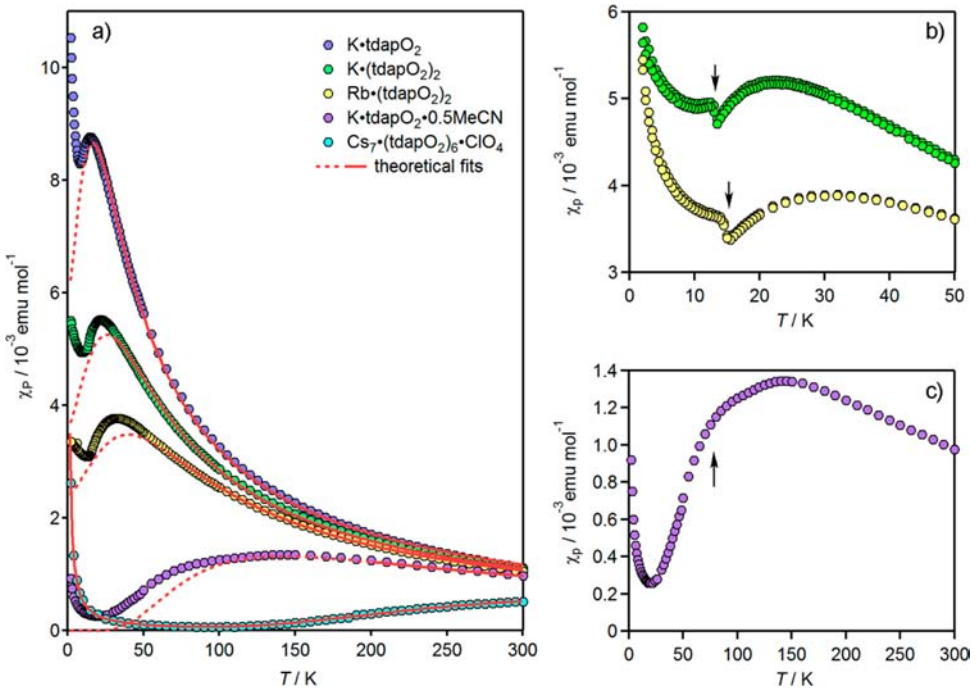

Figure 9. (a) Temperature dependence of χ_p of the alkali-metal salts of $tdapO_2$ under 3 T. Red curves show the theoretical fits to the experimental data at high temperatures, with extrapolation to low temperatures depicted as broken lines. (b) Magnetic anomalies in K·$(tdapO_2)_2$ and Rb·$(tdapO_2)_2$ observed under 0.05 T. (c) Magnetic anomaly in K·$tdapO_2$·0.5MeCN.

High-Temperature Behavior of Alkali-Metal Salts. Figure 9a shows the temperature dependence of the paramagnetic susceptibility χ_p for the alkali-metal salts of $tdapO_2$. The magnetic behaviors of K·$tdapO_2$ (blue circle) and K·$(tdapO_2)_2$ (green circle) can be explained as a 1D antiferromagnetic chain. The red curves fitted to their plots are theoretical curves from the Bonner–Fisher model[21,22] with the spin Hamiltonian in zero field: $H = -2J\Sigma S_i \cdot S_{i+1}$, where J is the exchange integral (see eq S1, Supporting Information). The parameters are $J/k_B = -13 \pm 1$ K for K·$tdapO_2$ and -20 ± 1 for K·$(tdapO_2)_2$, where k_B is the Boltzmann constant. The deviations from the theoretical curves at low temperatures are caused by the presence of Curie defects. The dependence of Rb·$(tdapO_2)_2$ (yellow) is similar to that of K·$(tdapO_2)_2$, but the former indicates a stronger antiferromagnetic exchange constant of $J/k_B = -29 \pm 1$ K. Both salts exhibit antiferromagnetic ordering, as will be shown in a later section. K·$tdapO_2$·0.5MeCN and Cs_7·$(tdapO_2)_6$·ClO_4 form alternating 1D chain structures in their crystals. The violet and light blue circles in Figure 9a depict the temperature dependence of χ_p for K·$tdapO_2$·0.5MeCN and Cs_7·$(tdapO_2)_6$·ClO_4, respectively, where the molar unit is defined to include 1 M of $tdapO_2$, namely, (1/6)[Cs_7·$(tdapO_2)_6$·ClO_4] for the latter salt. The χ_p values of K·$tdapO_2$·0.5MeCN show a gradual increase with a decrease in temperature from 300 K and form a broad maximum around 150 K. Further cooling makes a quick increase below 10 K due to Curie defects. Figure 9c shows the temperature dependence of χ_p for K·$tdapO_2$·0.5MeCN, which is enlarged from Figure 9a. The temperature dependence of χ_p shows a small anomaly at 80 K, which is considered to be a structural phase transition. A detailed structural study at low temperatures is in progress. In contrast, the χ_p of Cs_7·$(tdapO_2)_6$·ClO_4 shows a gradual decrease with a decrease in temperature from 300 K. After passing through a broad minimum around 100 K, the value of χ_p shows a quick increase below 30 K. The latter behavior can be explained as Curie defects of $C_{def} = 3.7 \times 10^{-3}$ emu mol^{-1} K. The behavior of K·$tdapO_2$·0.5MeCN in the range between 200 and 300 K, and that of Cs_7·$(tdapO_2)_6$·ClO_4 between 30 and 300 K can be fitted to the Bleaney–Bowers model[21,23] (see eq S2 with $H = -2JS_1 \cdot S_2$, Supporting Information) with the following fitting parameters: $g = 2.0 \pm 0.1$ and $J/k_B = -110 \pm 10$ K for K·$tdapO_2$·0.5MeCN, and $g = 2$ (fixed) and $J/k_B = -310 \pm 10$ K for Cs_7·$(tdapO_2)_6$·ClO_4.

Low-Temperature Behavior of Alkali-Metal Salts. The temperature dependences of χ_p for K·$(tdapO_2)_2$ and Rb·$(tdapO_2)_2$ in the temperature range below 60 K are shown in Figure 9b in an enlarged scale. The values of χ_p for the former and latter exhibit small jumps at 12 and 15 K, respectively, with a decrease in temperature. No hysteresis was associated with these anomalies. Their magnetization curves at 2 K show remnant magnetization, indicating that these anomalies are caused by antiferromagnetic ordering with spin canting (Figures S12 and S13, Supporting Information).

$(NH_4)_2$·$tdapO_2$·I and Hppda·$tdapO_2$·MeCN. Figure 10 shows the temperature dependence of χ_pT for $(NH_4)_2$·$tdapO_2$·I (blue circle) and Hppda·$tdapO_2$·MeCN (green circle). When the temperature decreases from 300 K, χ_pT of $(NH_4)_2$·$tdapO_2$·I exhibits a gradual increase down to 30 K. After passing a broad maximum, χ_pT decreases quickly. This behavior indicates the coexistence of ferromagnetic and antiferromagnetic interactions, the former of which should be stronger than the latter. Hppda·$tdapO_2$·MeCN exhibits a similar behavior, with a sharper maximum at 10 K. Since the crystal structure of $(NH_4)_2$·$tdapO_2$·I consists of alternated π stacking, this temperature dependence can be interpreted in terms of a ferromagnetic dimer, with weak antiferromagnetic interdimer coupling (see eq S3 with $H = -2J_1S_1 \cdot S_2 - 2zJ_2(\langle S_1^z \rangle \cdot S_2^z + \langle S_2^z \rangle \cdot S_1^z)$, Supporting Information).[24] The solid curve in Figure 10 is the best fit with $g = 1.94 \pm 0.10$, $J_1/k_B = 24 \pm 1$ K, and $zJ_2/k_B =$

dx.doi.org/10.1021/ic401078z | Inorg. Chem. 2013, 52, 9921–9930

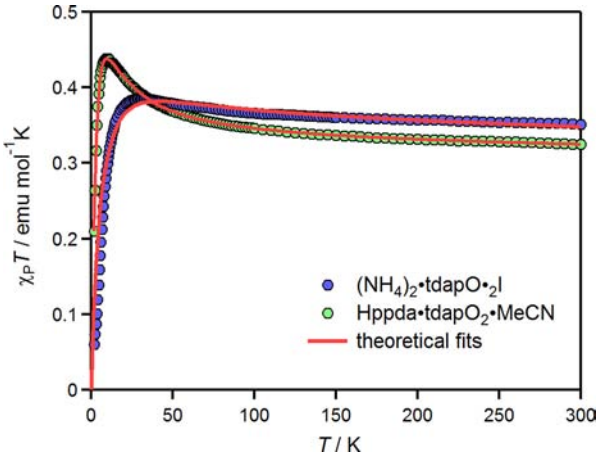

Figure 10. Temperature dependence of the $\chi_p T$ of ammonium salts. Red curves show the theoretical fits.

−7.9 ± 0.1 K, where J_1 and J_2 express the intradimer ferromagnetic coupling constant and the interdimer antiferromagnetic coupling constant, respectively, and z is the number of the nearest-neighbors connected by J_2. The experimental data are well reproduced by this model. It is clear that the $tdapO_2$ radical−anion has the potential to yield both ferromagnetic and antiferromagnetic intermolecular interactions.

The temperature dependence of $\chi_p T$ for Hppda·$tdapO_2$·MeCN, which includes a regular π stacking in its solids, can be interpreted in terms of a ferromagnetic 1D chain J_1 and a weak antiferromagnetic interchain coupling J_2 (see eq S4 with $H = -2J_1\Sigma S_i \cdot S_{i+1}$ and a molecular mean-field correction, Supporting Information).[21,22b,25] The solid curve in Figure 10 is the best fit with $g = 1.84 \pm 0.10$, $J_1/k_B = 5.6 \pm 0.1$ K, and $zJ_2/k_B = -2.2 \pm 0.1$ K. The g factors of $(NH_4)_2$·$tdapO_2$·I and Hppda·$tdapO_2$·MeCN are a little bit smaller than the expected value ($g = 2$), though we repeated the experiments several times. This was perhaps due to lattice defects of the protons and/or a partial decomposition of the radical species.

VI. COMPUTATIONAL CALCULATIONS

It is quite remarkable that the $tdapO_2$ radical−anion gives rise to magnetic networks characterized by exchange coupling constants that significantly vary from antiferromagnetic $J/k_B = -310$ K to ferromagnetic $J/k_B = 24$ K values (see Table 1, Figure 11). To understand the extent of this range, we carried out ab initio DDCI calculations for the exchange interactions of various $tdapO_2$ radical−anion dimers, which were based on the different molecular packings found in the presented crystal structures. Out of the low-energy spectroscopy of the dimeric units, the exchange coupling constants J, effective hopping integral t, on-site repulsion U, and direct exchange K were extracted at the DDCI level and are summarized in Table 1.

As expected, the magnetic orbitals are the in-phase and out-of-phase linear combinations of the singly occupied MOs (SOMOs) localized on each radical (Figure 12). In light of the localized character of the spin densities, the relative position of the radicals (i.e., the three-dimensional arrangement) becomes a determining factor governing the magnetic interactions. Table 1 and Figure 11 show the evolution of the J value with respect to the interplanar distance between the two radicals of the dimers studied in the present work. The significant dependence of the exchange coupling constant on this structural parameter is very instructive and indicates that the overlap between the monomers plays a major role in defining the magnetic character of these materials. In addition, a large influence of the slippage between the two radicals has also been reported previously.[26]

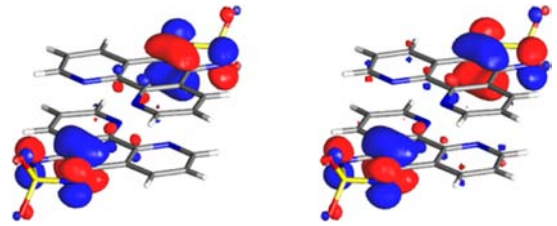

Figure 12. Active MOs resulting from a CAS[2,2]SCF calculation performed for the triplet state of a dimer extracted from the crystal structure of K·$tdapO_2$.

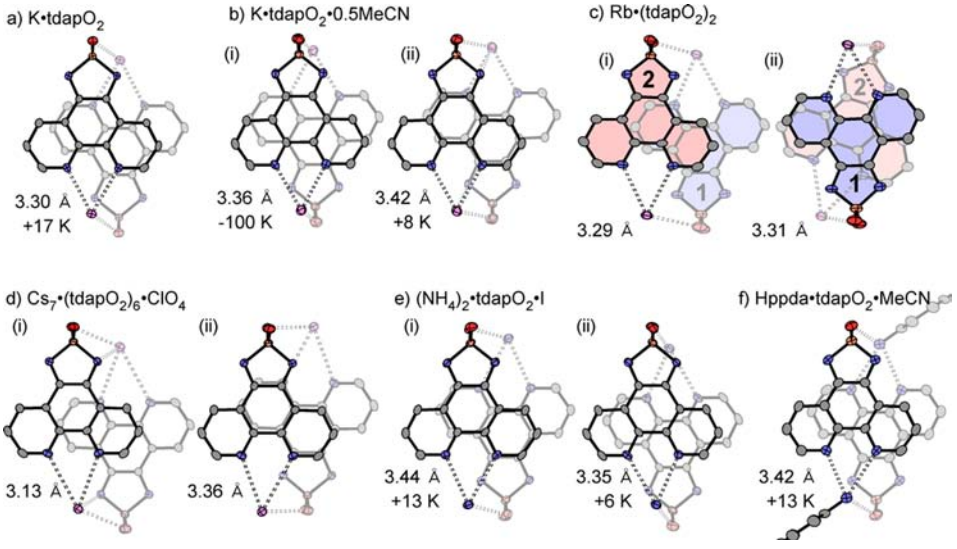

Figure 11. π overlaps between neighboring $tdapO_2$ radical−anions, and corresponding interplanar distances and calculated magnetic exchange coupling constants.

dx.doi.org/10.1021/ic401078z | Inorg. Chem. 2013, 52, 9921−9930

Furthermore, the spin polarization effects are also expected to play a role, and these effects might be modulated by introduction of oxygen atoms in the organic structure. Next, we will focus on the tuning of parameters produced under different crystallization conditions and chemical modifications of the radical skeleton.

The calculated exchange coupling constants values turned out to be in good agreement with the experimental estimates (Table 1), despite some qualitative deviations observed in the paramagnetic vicinity regime. Only one of the calculated radical pairs exhibits relatively strong antiferromagnetic behavior (−100 K), which seems to be highly controlled by the presence of oxygen atoms. Indeed, the comparison between Hppda·tdapO$_2$·MeCN and the hypothetical Hppda·tdap·MeCN (lacking oxygen atoms on the thiadiazole ring) is rather instructive. Removal of the oxygen atoms shifts the magnetic behavior from ferro- (13 K) to antiferromagnetic (−4 K). One may also take advantage of the partitioning offered by extraction of these parameters to shed some light onto these modulations.

The on-site Coulomb repulsion U is mostly governed by the radical characteristics regarding its chemical constitution and accounts for the electron−electron repulsive energy when both electrons are localized on the same subunit. The resulting electronic structures are designated ionic forms since they can be schematically written as tdapO$_2$(+)···tdapO$_2$(−). In contrast, the electronic configurations resulting from the single occupancy of the local magnetic orbitals are called neutral. The latter are present in both singlet and triplet states, whereas the former are absent in the triplet state. Typically, the non-negligible weight of ionic structures is the leading factor that drives biradical species to become antiferromagnetic. Nonetheless, it must be noted that a rather different origin for antiferromagnetism has recently been reported for Ullman's biradical.[14d]

Rota et al. showed that the on-site repulsion U is almost constant as long as the material building units are unchanged.[26b] However, we must stress that removal of the electron-withdrawing oxygen atoms leads to a ca. 3800 K increase of U in the hypothetical Hppda·tdap·MeCN radical as compared to Hppda·tdapO$_2$·MeCN. This shift is in agreement with the ca. −1.5 V shift of the reduction potential to smaller values on the CV curves. Such variation of U is overtaken by a significant increase of the hopping integral t (from 85 to 791 K), which drives the hypothetical Hppda·tdap·MeCN into the antiferromagnetic regime. It must be noted that the variation of t caused by removal of oxygen atoms is opposite to what was observed for nitro addition on a neutral verdazyl-based biradical.[27] This inconsistent behavior between these two organic radical materials might be caused by the different electrostatic character of the anionic tdap and the neutral verdazyl material.

To check whether the impact of oxygen atoms on the J value is due to the spin polarization (SP) effects, we carried out CI calculations involving only those excitations responsible for this effect (class-partitioned CI calculations).[28] Spin polarization produces a remarkable increase of the ferromagnetic contribution in both systems. However, the interaction of these SP excitations with the 1h determinants (all of them present in the DDCI space) provides a differential effect for these two systems: an antiferromagnetic coupling is obtained for the hypothetical Hppda·tdap·MeCN, while the Hppda·tdapO$_2$·MeCN system remains ferromagnetic, with a large coupling constant. Inspection of the singlet wave functions suggests that the single excitations from the (SOMO-1) orbitals (Figure S14, Supporting Information) to the active ones are responsible for this differential effect in the tdap dimer. For the oxygen-containing system, the equivalent orbitals are highly stabilized and so the corresponding 1h excitations are high in energy and make a negligible antiferromagnetic contribution to the coupling.

We also analyzed the structure of the lowest-lying singlet state wave function of dimeric systems based on the hypothetical Hppda·tdap·MeCN and Hppda·tdapO$_2$·MeCN. At the best level of calculation (DDCI), the ratio between the weights of the ionic forms and the neutral ones is increased by ca. 50 upon removal of oxygen atoms. A general trend in the series of compounds is that the antiferromagnetic contribution tends to be negligible due to the relatively small t value. The dimeric system based on K·tdapO$_2$·0.5MeCN (i) is remarkable since the hopping integral t is at least six times larger than the values of other inspected radical pairs, and this is the only exception among the series of analyzed systems in which the large interplanar distance does not correlate with a weaker antiferromagnetic J value (Table 1).

VII. CONCLUSION

In previous paper, we prepared novel acceptor molecule tdapO$_2$ and its radical−anion salts which have unique features such as stability and delocalization of unpaired electron and good coordination and proton acceptor ability. In the present paper, we developed stable tdapO$_2$ radical−anion salts of alkali-metal and ammonium salts and investigated their magnetic properties. While the major magnetic interactions of alkali-metal salts (K·tdapO$_2$, K·tdapO$_2$·0.5MeCN, K·(tdapO$_2$)$_2$, Rb·(tdapO$_2$)$_2$, and Cs$_7$·(tdapO$_2$)$_6$·ClO$_4$) are antiferromagnetic, those of ammonium salts ((NH$_4$)$_2$·tdapO$_2$·I and Hppda·tdapO$_2$·MeCN) are ferromagnetic. This variety of magnetic interactions could be derived from the diverse crystal structures formed by coordination and hydrogen bonding. Theoretical calculations of the magnetic interactions of dimeric units built on nearest-neighbor radicals indicate that the ferromagnetic interactions are governed by relatively small t values. This result and the dependence of J on the interplanar distance suggest that the ferro- and antiferromagnetic interactions are strongly governed by the overlap between the two radical−anion species. The hypothetical oxygen-less analogue system shows that the presence of oxygen bonded to sulfur largely decreases the t value. Therefore, it is concluded that introduction of the oxygen atoms reduces the antiferromagnetic interactions.

■ ASSOCIATED CONTENT

Supporting Information

X-ray crystallographic files in CIF format, molecular structures, synthesis of neutral and divalent tdapO$_2$ intermolecular compounds, theoretically and experimentally calculated spin populations, detailed crystal structures and crystallographic data for intermolecular compounds, magnetization curves of K·(tdapO$_2$)$_2$ and Rb·(tdapO$_2$)$_2$, and spin Hamiltonian and theoretical equations. This material is available free of charge via the Internet at http://pubs.acs.org.

■ AUTHOR INFORMATION

Corresponding Author

*E-mail: awaga@mbox.chem.nagoya-u.ac.jp.

Present Address

‡Graduate School of Advanced Integration Science, Chiba University.

Notes

The authors declare no competing financial interest.

■ ACKNOWLEDGMENTS

Financial support has been provided in the form of a Grant-in-Aid for Scientific Research from the Ministry of Education, Culture, Sports, Science, and Technology (MEXT) of Japan, by the Laboratoire d'Excellence on Chemistry of Complex Systems (LabEx-CSC, Strasbourg), and by the Spanish Ministry of Science and Innovation (Project No. CTQ2009-07767).

■ REFERENCES

(1) (a) Kobayashi, H.; Kobayashi, A.; Tajima, H. *Chem. Asian J.* **2011**, *6*, 1688−1704. (b) Miller, J. S. *Chem. Soc. Rev.* **2011**, *40*, 3266−3296. (c) Awaga, K.; Tanaka, T.; Shirai, T.; Fujimori, M.; Suzuki, Y.; Yoshikawa, H.; Fujita, W. *Bull. Chem. Soc. Jpn.* **2006**, *79*, 25−34. (d) Gütlich, P.; Koningsbruggen, P. J.; Renz, F. *Struct. Bonding (Berlin)* **2004**, *107*, 27−75. (e) Sato, O.; Tao, J.; Zhang, Y. *Angew. Chem., Int. Ed.* **2007**, *46*, 2152−2187. (f) Gatteschi, D. *Adv. Mater.* **1994**, *6*, 635−645.

(2) In *Semiconductors and semimetals*; Conwell, E., Ed.; Academic Press: New York, 1988; Vol. *27*.

(3) (a) Kaim, W.; Moscherosch, M. *Coord. Chem. Rev.* **1994**, *129*, 157−193. (b) Lopez, N.; Zhao, H.; Ota, A.; Prosvirin, A. V.; Reinheimer, E. W.; Dunbar, K. R. *Adv. Mater.* **2010**, *22*, 986−989. (c) Kato, R.; Kobayashi, H.; Kobayashi, A. *J. Am. Chem. Soc.* **1989**, *111*, 5224−5232.

(4) (a) Caram, J. A.; Mirifico, M. V.; Vasini, E. *J. Electrochim. Acta* **1994**, *39*, 939−945. (b) Caram, J. A.; Mirifico, M. V.; Aimone, S. L.; Vasini, E. J. *Can. J. Chem.* **1996**, *74*, 1564−1571. (c) Caram, J. A.; Mirifico, M. V.; Aimone, S. L.; Piro, O. E.; Castellano, E. E.; Vasini, E. J. *J. Phys. Org. Chem.* **2004**, *17*, 1091−1098. (d) Mirifico, M. V.; Caram, J. A.; Gennaro, A. M.; Cobos, C. J.; Vasini, E. J. *J. Phys. Org. Chem.* **2009**, *22*, 964−970.

(5) Shuku, Y.; Suizu, R.; Awaga, K. *Inorg. Chem.* **2011**, *50*, 11859−11861.

(6) Conte, G.; Bortoluzzi, A. J.; Gallardo, H. *Synthesis* **2006**, *23*, 3945−3947.

(7) *CrystalClear & CrystalStructure*, Rigaku/MSC: The Woodlands, TX, 2005.

(8) Sheldrick, G. M.SHELX-97 *Program for the Refinement of Crystal Structure*; University of Göttingen: Germany,1997.

(9) (a) Calzado, C. J.; Cabrero, J.; Malrieu, J.-P.; Caballol, R. *J. Chem. Phys.* **2002**, *116*, 2728−2746. (b) Calzado, C. J.; Cabrero, J.; Malrieu, J.-P.; Caballol, R. *J. Chem. Phys.* **2002**, *116*, 3985−4000.

(10) Roos, B. O.; Taylor, P. R.; Siegbahn, P. E. M. *Chem. Phys.* **1980**, *48*, 157.

(11) (a) Aquilante, F.; De Vico, L.; Ferré, N.; Ghigo, G.; Malmqvist, P.-A.; Neogrády, P.; Pedersen, T. B.; Pitoňák, M.; Reiher, M.; Roos, B. O.; Serrano-Andrés, L.; Urban, M.; Veryazov, V.; Lindh, R. *J. Comput. Chem.* **2010**, *31*, 224−247. (b) Roos, B. O.; Lindh, R.; Malmqvist, P.-A.; Veryazov, V.; Widmark, P.-O. *J. Phys. Chem. A* **2004**, *108*, 2851.

(12) Barandiarán, Z.; Seijo, L. *J. Chem. Phys.* **1988**, *89*, 5739.

(13) (a) Miralies, J.; Malrieu, J.; Caballol, R. *Chem. Phys.* **1991**, *153*, 25−37. (b) Amor, N. B.; Maynau, D. *Chem. Phys. Lett.* **1998**, *286*, 211−220.

(14) (a) Rota, J.-B.; Calzado, C. J.; Train, C.; Robert, V. *J. Chem. Phys.* **2010**, *132*, 154702. (b) Oms, O.; Rota, J.-B.; Norel, L.; Calzado, C. J.; Rousselière, H.; Train, C.; Robert, V. *Eur. J. Inorg. Chem.* **2010**, 5373−5378. (c) Vérot, M.; Bréfuel, N.; Pécaut, J.; Train, C.; Robert, V. *Chem. Asian J.* **2012**, *7*, 380−386. (d) Angeli, C.; Calzado, C. J.; Graaf, C. de; Caballol, R. *Phys. Chem. Chem. Phys.* **2011**, *13*, 14617−14628.

(15) (a) Chambers, J. Q. In *The chemistry of the quinonoid compounds*; Patai, S., Ed.; John Wiley & Sons: New York, 1974. (b) Peover, M. E. *J. Chem. Soc.* **1962**, 4540−4549. (c) Davis, K. M. C.; Hammond, P. R.; Peover, M. E. *Trans. Faraday Soc.* **1965**, *61*, 1516−1522. (d) Ryba, O.; Pilar, J.; Petranek, J. *Collect. Czech. Chem. Commun.* **1968**, *33*, 26−34.

(16) Lim, B. S.; Fomitchev, D. V.; Holm, R. H. *Inorg. Chem.* **2001**, *40*, 4257−4262.

(17) (a) McConnell, H. M. *J. Chem. Phys.* **1958**, *28*, 1188−1192. (b) McConnell, H. M.; Strathdee, J. *Mol. Phys.* **1959**, *2*, 129−138.

(18) Talcott, C. L.; Myers, R. J. *Mol. Phys.* **1967**, *12*, 549−567.

(19) Carrington, A.; Dossantosveiga, J. *Mol. Phys.* **1962**, *5*, 21−29.

(20) Ramirez, A. P. *Annu. Rev. Mater. Sci.* **1994**, *24*, 453−480.

(21) Kahn, O. *Molecular Magnetism*; Wiley-VCH: Weinheim, 1993.

(22) (a) Bonner, J. C.; Fisher, M. E. *Phys. Rev.* **1964**, *135*, A640−A658. (b) Estes, W. E.; Gavel, D. P.; Hatfield, W. E.; Hodgson, D. J. *Inorg. Chem.* **1978**, *17*, 1415−1421.

(23) Bleaney, B.; Bowers, K. D. *Proc. R. Soc. London, Ser. A* **1952**, *214*, 451−465.

(24) Awaga, K.; Okuno, T.; Yamaguchi, A.; Hasegawa, M.; Inabe, T.; Maruyama, Y.; Wada, N. *Phys. Rev. B* **1994**, *49*, 3975−3981.

(25) Baker, G. A.; Rushbrooke, G. S.; Gilbert, H. E. *Phys. Rev.* **1964**, *135*, A1272−A1277.

(26) Norel, L.; Rota, J.-B.; Chamoreau, L.-M.; Pilet, G.; Robert, V.; Train, C. *Angew Chem. Int. Ed.* **2011**, *50*, 7128−7131. (b) Rota, J.-B.; Guennic, C. Le; Robert, V. *Inorg. Chem.* **2010**, *49*, 1230−1237. (c) Leitch, A. A.; Yu, X.; Winter, S. M.; Secco, R. A.; Dube, P. A.; Oakley, R. T. *J. Am. Chem. Soc.* **2009**, *131*, 7112−7125.

(27) Domingo, A.; Vérot, M.; Mota, F.; de Graaf, C.; Novoa, J. J.; Robert, V. *Phys. Chem. Chem. Phys.* **2013**, DOI: 10.1039/C3CP44647F.

(28) Calzado, C. J.; Angeli, C.; Taratiel, D.; Caballol, R.; Malrieu, J. P. *J. Chem. Phys.* **2009**, *131*, 044327.